

ARMY RESEARCH LABORATORY



Modeling Damage and Fragmentation in Concrete

by John D. Clayton

ARL-RP-169

April 2007

A reprint from the *Sixth International Conference on Composite Science and Technology*,
pp. 1–15, Durban, South Africa, 22–24 January 2007.

NOTICES

Disclaimers

The findings in this report are not to be construed as an official Department of the Army position unless so designated by other authorized documents.

Citation of manufacturer's or trade names does not constitute an official endorsement or approval of the use thereof.

Destroy this report when it is no longer needed. Do not return it to the originator.

Army Research Laboratory

Aberdeen Proving Ground, MD 21005-5069

ARL-RP-169

April 2007

Modeling Damage and Fragmentation in Concrete

**John D. Clayton
Weapons and Materials Research Directorate, ARL**

A reprint from the *Sixth International Conference on Composite Science and Technology*,
pp. 1–15, Durban, South Africa, 22–24 January 2007.

REPORT DOCUMENTATION PAGE			<i>Form Approved OMB No. 0704-0188</i>	
<p>Public reporting burden for this collection of information is estimated to average 1 hour per response, including the time for reviewing instructions, searching existing data sources, gathering and maintaining the data needed, and completing and reviewing the collection information. Send comments regarding this burden estimate or any other aspect of this collection of information, including suggestions for reducing the burden, to Department of Defense, Washington Headquarters Services, Directorate for Information Operations and Reports (0704-0188), 1215 Jefferson Davis Highway, Suite 1204, Arlington, VA 22202-4302. Respondents should be aware that notwithstanding any other provision of law, no person shall be subject to any penalty for failing to comply with a collection of information if it does not display a currently valid OMB control number.</p> <p>PLEASE DO NOT RETURN YOUR FORM TO THE ABOVE ADDRESS.</p>				
1. REPORT DATE (DD-MM-YYYY) April 2007	2. REPORT TYPE Reprint	3. DATES COVERED (From - To) 22–24 January 2007		
4. TITLE AND SUBTITLE Modeling Damage and Fragmentation in Concrete			5a. CONTRACT NUMBER	
			5b. GRANT NUMBER	
			5c. PROGRAM ELEMENT NUMBER	
6. AUTHOR(S) John D. Clayton			5d. PROJECT NUMBER WHPR01E	
			5e. TASK NUMBER	
			5f. WORK UNIT NUMBER	
7. PERFORMING ORGANIZATION NAME(S) AND ADDRESS(ES) U.S. Army Research Laboratory ATTN: AMSRD-ARL-WM-TD Aberdeen Proving Ground, MD 21005-5069			8. PERFORMING ORGANIZATION REPORT NUMBER ARL-RP-169	
9. SPONSORING/MONITORING AGENCY NAME(S) AND ADDRESS(ES)			10. SPONSOR/MONITOR'S ACRONYM(S)	
			11. SPONSOR/MONITOR'S REPORT NUMBER(S)	
12. DISTRIBUTION/AVAILABILITY STATEMENT Approved for public release; distribution is unlimited.				
13. SUPPLEMENTARY NOTES A reprint from the <i>Sixth International Conference on Composite Science and Technology</i> , pp. 1–15, Durban, South Africa, 22–24 January 2007.				
14. ABSTRACT A theory combining nonlinear continuum elasticity, inelasticity, thermodynamics, damage mechanics, and fragmentation is formulated. The model is applied to study concrete subjected to high rate loading as occurs during ballistic impact. Two thermodynamically motivated methods are postulated within this theoretical framework for quantitatively characterizing the mass and velocity distributions of the post-impact debris field, one based upon a local energy balance and a second following global entropy maximization. Here the concrete, a composite mixture of mortar and granite aggregate, is regarded as a homogeneous continuum prior to fragmentation. However, the composite nature of the microstructure directly influences model parameters dictating the mean fragment dimension, here specifically related to the coarse aggregate size. Standard continuum elements represent the intact solid and particles describe eroded material in numerical implementation of the model. The impact of a metal sphere on a thin concrete target, and the subsequent motion of the resulting cloud of concrete fragment debris, are simulated. Fragment size, speed, and kinetic energy statistics predicted by the two methods are compared.				
15. SUBJECT TERMS damage mechanics, thermodynamics, fragmentation, concrete				
16. SECURITY CLASSIFICATION OF: UNCLASSIFIED		17. LIMITATION OF ABSTRACT UL	18. NUMBER OF PAGES 22	19a. NAME OF RESPONSIBLE PERSON John D. Clayton
a. REPORT UNCLASSIFIED	b. ABSTRACT UNCLASSIFIED			c. THIS PAGE UNCLASSIFIED

MODELING DAMAGE AND FRAGMENTATION IN CONCRETE

John D. Clayton

U.S. Army Research Laboratory, AMSRD-ARL-WM-TD, APG, MD, USA 21005-5069
jclayton@arl.army.mil

ABSTRACT

A theory combining nonlinear continuum elasticity, inelasticity, thermodynamics, damage mechanics, and fragmentation is formulated. The model is applied to study concrete subjected to high rate loading as occurs during ballistic impact. Two thermodynamically motivated methods are postulated within this theoretical framework for quantitatively characterizing the mass and velocity distributions of the post-impact debris field, one based upon a local energy balance and a second following global entropy maximization. Here the concrete, a composite mixture of mortar and granite aggregate, is regarded as a homogeneous continuum prior to fragmentation. However, the composite nature of the microstructure directly influences model parameters dictating the mean fragment dimension, here specifically related to the coarse aggregate size. Standard continuum elements represent the intact solid and particles describe eroded material in numerical implementation of the model. The impact of a metal sphere on a thin concrete target, and the subsequent motion of the resulting cloud of concrete fragment debris, are simulated. Fragment size, speed, and kinetic energy statistics predicted by the two methods are compared.

Keywords: damage mechanics, thermodynamics, fragmentation, concrete.

1. INTRODUCTION

Urban structural materials such as concrete, mortar, and cinder block may undergo complex set of deformation mechanisms when subjected to impact loading. Since they nominally contain significant initial porosity, for example on the order of 10-20% in standardized concretes [1, 2], these materials are labeled here as 'crushable'. The goal of the present study is development and implementation of a kinematically and thermodynamically self-consistent theory accounting for coupled deformation, damage, and fragmentation mechanisms, specifically amenable to brittle crushable solids. In such materials, initial porosity induces pressure dependence in the effective bulk modulus, with the stiffness of the material increasing as the pores are compacted. Additional difficulty in precisely modeling concrete behavior follows from the variability in mechanical properties such as flow stress and fracture toughness with microstructure constituents [3], processing conditions, and age.

Previous modeling approaches most relevant to the present work are mentioned here. Holmquist et al. [4] developed a constitutive model, with the pressure-volume response following data from [1], and a plasticity and damage framework similar, yet not identical, to one used previously for metallic materials [5], with failure criteria based on cumulative strain measures [6]. The numerical approach followed here is that of Johnson et al. [7, 8], whereby continuum finite elements are converted via a Generalized Particle Algorithm (GPA) to particle nodes when specified erosion criteria are met. However, information regarding sizes of individual fragments has not historically been available from Smooth Particle Hydrodynamics (SPH) or GPA, since the mass of each particle is simply the nodal mass, which in turn depends upon the mesh density. The issue is resolved here by incorporating thermodynamics-based fragmentation theory into the constitutive framework enabling calculation of non-uniform mass distributions.

Two methods are derived in the present work for calculating fragment size and velocity distributions, both compatible with the laws of thermodynamics and momentum

conservation. The first follows from on a local energy balance similar to that of Grady [9] and Johnson & Cook [10], but newly applied to the class of concrete-like materials in a manner more consistent with the bulk constitutive model. The distribution of fragment masses is found in practice via consideration of an energy balance with regards to the deformation history of converted particles in the simulation, with the velocity distribution of the fragments associated with that of the parent particles. In the second approach, a theory based on entropy maximization and classical statistical physics is implemented [11, 12]. In this approach, a new joint probability distribution function for fragment mass and velocity is derived consistent with energy and linear momentum conservation

The following notation applies. Cartesian coordinates are used throughout, with summation implied over repeated indices. Vectors and tensor quantities are represented with boldface type, while scalars and individual components of tensors are written in italics. Juxtaposition implies summation over two repeated adjacent indices (e.g. $(\mathbf{AB})_a^b = A_{ac}B^{cb}$). The scalar product of vectors is represented by “•” (e.g. $\mathbf{a} \cdot \mathbf{b} = a^a b_a$). The colon denotes contraction over repeated pairs of indices (e.g. $\mathbf{A} : \mathbf{B} = \text{tr}(\mathbf{A}^T \mathbf{B}) = A_{ab}B^{ab}$, where ‘tr’ is the trace operation, and $\mathbf{C} : \mathbf{A} = C^{abcd} A_{cd}$). Superposed -1, T , and “•” denote inverse, transpose, and material time derivative, respectively.

2. CONTINUUM THERMOMECHANICS

The theoretical framework postulated here differs from many existing models in its implementation of a multiplicative decomposition of the deformation gradient into elastic and inelastic components [13] and its strict consistency with the balance laws of continuum mechanics and thermodynamics. More specifically, thermodynamic relations and evolution equations for porosity and damage are formulated in the spirit of Coleman & Noll [14] and Coleman & Gurtin [15].

The deformation gradient \mathbf{F} is split multiplicatively as

$$\mathbf{F} = \partial \mathbf{x} / \partial \mathbf{X} = \mathbf{F}^E \mathbf{F}^D, \quad F_{.A}^a = \partial x^a / \partial X^A = F_{.\alpha}^{Ea} F_{.A}^{D\alpha}, \quad (1)$$

where \mathbf{x} and \mathbf{X} are spatial and reference coordinates in three dimensional Cartesian space, \mathbf{F}^E is the recoverable elastic deformation, and \mathbf{F}^D is the irreversible deformation associated with defects such as micro-cracks and voids within the material. Deformation maps and corresponding material configurations corresponding to Eq. (1) are depicted in Fig. 1. The velocity gradient \mathbf{L} follows as

$$\mathbf{L} = \partial \dot{\mathbf{x}} / \partial \mathbf{X} = \underbrace{\dot{\mathbf{F}}^E \mathbf{F}^{E-1}}_{\mathbf{L}^E} + \underbrace{\mathbf{F}^E \dot{\mathbf{F}}^D \mathbf{F}^{D-1} \mathbf{F}^{E-1}}_{\mathbf{L}^D}. \quad (2)$$

Irreversible volumetric deformation associated with pore collapse in crushable materials is described by

$$\varphi = J^{D-1} - 1, \quad J^D = \det \mathbf{F}^D, \quad (3)$$

where φ is the volume reduction upon crushing, positive when the volume is reduced. The total inelastic velocity gradient from (2) then becomes

$$\mathbf{L}^D = \mathbf{F}^E \dot{\mathbf{F}}^D \mathbf{F}^{D-1} \mathbf{F}^{E-1} = \hat{\mathbf{L}}^D - \dot{\varphi} (1 + \varphi)^{-1} \mathbf{1}, \quad (4)$$

where $\hat{\mathbf{L}}^D$ is the deviatoric inelastic velocity gradient in spatial configuration B and $\mathbf{1}$ is the identity tensor. An elastic strain tensor and a scalar measure of volumetric elastic strain in the intermediate configuration \bar{B} of Fig. 1 are defined, respectively, as

$$2\mathbf{E}^E = \mathbf{F}^{ET}\mathbf{F}^E - \mathbf{1}, \quad \vartheta_E = \text{tr}\mathbf{E}^E. \quad (5)$$

Standard balances of mass, linear and angular momentum are written in localized form as

$$\rho_0 = \rho J = \rho \det \mathbf{F}, \quad \text{div}\boldsymbol{\sigma} + \mathbf{f} = \rho \ddot{\mathbf{x}}, \quad \boldsymbol{\sigma} = \boldsymbol{\sigma}^T, \quad (6)$$

where \mathbf{f} is the body force vector per unit spatial volume, $\boldsymbol{\sigma}$ is the Cauchy stress tensor, and div denotes divergence in the spatial frame. The local spatial energy balance is

$$\rho \dot{e} = \boldsymbol{\sigma} : \mathbf{L} - \text{div}\mathbf{q}, \quad (7)$$

with e the internal energy per unit mass and \mathbf{q} the heat flux. The local second law of thermodynamics is written

$$\boldsymbol{\sigma} : \mathbf{L} - \theta^{-1} \mathbf{q} \cdot \partial_x \theta \geq \rho (\psi + \dot{\eta}), \quad (8)$$

where θ is the absolute temperature, η is the specific entropy per unit mass, and the Helmholtz free energy is $\psi = e - \theta\eta$. The spatial gradient operator is denoted by ∂_x .

The Helmholtz free energy, on a per unit mass basis, exhibits the following functional form:

$$\psi = \psi(\mathbf{E}^E, \varphi, \theta, D), \quad (9)$$

where D is a scalar internal state variable representing cumulative damage. Stress-strain and temperature-entropy relations are then deduced as

$$\boldsymbol{\sigma} = \mathbf{F}^E \rho \frac{\partial \psi}{\partial \mathbf{E}^E} \mathbf{F}^{ET}, \quad \eta = -\rho \frac{\partial \psi}{\partial \theta}. \quad (10)$$

The dissipation inequality (8) is then given by

$$\boldsymbol{\sigma} : \hat{\mathbf{L}}^D + \left(\frac{p}{1+\varphi} - \rho \frac{\partial \psi}{\partial \varphi} \right) \dot{\varphi} - \rho \frac{\partial \psi}{\partial D} \dot{D} \geq \theta^{-1} \mathbf{q} \cdot \partial_x \theta, \quad (11)$$

where the Cauchy pressure $3p = -\text{tr}\boldsymbol{\sigma}$. Assuming isotropic heat conduction in the spatial frame, i.e. $\mathbf{q} = -\kappa \partial_x \theta$, with κ the scalar thermal conductivity, and defining the specific heat parameter $\hat{c} = \partial e / \partial \theta = -\theta \partial^2 \psi / \partial \theta^2$, the energy balance can be written as

$$\rho \hat{c} \dot{\theta} = \boldsymbol{\sigma} : \mathbf{L}^D - \rho \left[\left(\frac{\partial \psi}{\partial \varphi} - \theta \frac{\partial^2 \psi}{\partial \theta \partial \varphi} \right) \dot{\varphi} - \left(\frac{\partial \psi}{\partial D} - \theta \frac{\partial^2 \psi}{\partial \theta \partial D} \right) \dot{D} + \theta \frac{\partial \psi}{\partial \theta \partial \mathbf{E}^E} : \dot{\mathbf{E}}^E \right] + \text{div}(\kappa \partial_x \theta). \quad (12)$$

In the present class of urban structural materials (e.g. concrete, mortar) \mathbf{F}^D is associated with micro-crack opening and sliding, as well as pore collapse during compression. Let ω represent the cumulative local micro-cracked area per unit intermediate volume. Further, let $D = \omega / \omega_c$, where ω_c is a material parameter denoting the maximum

sustainable crack density, and constrained by the restriction $0 \leq D \leq 1$. The specific free energy density is more specifically formulated as

$$\tilde{\rho}\psi = K(\vartheta_E, \varphi)\vartheta_E^2 + G(1-D)\hat{\mathbf{E}}^E : \hat{\mathbf{E}}^E + \Gamma(D) + Y(\theta), \quad (13)$$

where $\tilde{\rho} = \rho J^E$, K is the effective bulk modulus, G is the initial shear modulus, $\hat{\mathbf{E}}^E = \mathbf{E}^E - (\vartheta_E/3)\mathbf{1}$ is the elastic strain deviator, Γ accounts for energy of micro-cracks, and Y describes the specific heat content. In particular, the effective bulk modulus takes the form

$$K = \frac{1}{2}K_E \left(\frac{\varphi_L - \varphi}{\varphi_L} \right) + \left(\frac{1}{2}K_1 + \frac{1}{3}K_2\vartheta_E + \frac{1}{4}K_3\vartheta_E^2 \right) \frac{\varphi}{\varphi_L}, \quad (14)$$

where K_E is the initial elastic bulk modulus, φ_L is the maximum porosity reduction due to compressive pressure, and K_1 , K_2 , and K_3 determine the pressure-volume relationship for the fully dense material at locking, when $\varphi = \varphi_L$. The microcrack energy per unit volume is

$$-\Gamma = \gamma\omega = \left(K_C^2\omega_C / 2K_E \right) D, \quad (15)$$

where $\gamma = K_C^2 / 2K_E$ is the surface energy of fracture [16], with K_C the effective fracture toughness. Note that constant material properties are used in (15) as a first approximation.

The intermediate second Piola stress is given, following from (10), by

$$\mathbf{S} = \tilde{\rho} \frac{\partial \psi}{\partial \mathbf{E}^E} = J^E \mathbf{F}^{E-1} \boldsymbol{\sigma} \mathbf{F}^{E-T}. \quad (16)$$

Then from (13) and (14), respectively, hydrostatic and deviatoric parts of \mathbf{S} are

$$\tilde{p} = -\text{tr}\mathbf{S}/3 = -K_E\vartheta_E(\varphi_L - \varphi)/\varphi_L - \left(K_1\vartheta_E + K_2\vartheta_E^2 + K_3\vartheta_E^3 \right) \varphi/\varphi_L, \quad (17)$$

$$\hat{\mathbf{S}} = \mathbf{S} + \tilde{p}\mathbf{1} = 2(1-D)G\hat{\mathbf{E}}^E. \quad (18)$$

The Cauchy pressure is $-3p = \text{tr}\boldsymbol{\sigma} = J^{E-1}F_{,\alpha}^{E,a}S^{\alpha\beta}F_{,\beta}^E$.

Deviatoric plasticity is controlled by the flow potential Φ , equated here with the scalar effective deviatoric stress $\bar{\sigma} = \sqrt{(3/2)\hat{\boldsymbol{\sigma}}:\hat{\boldsymbol{\sigma}}}$:

$$\hat{\mathbf{L}}^D = \lambda \frac{\partial \Phi}{\partial \hat{\boldsymbol{\sigma}}}, \quad \Phi = \left[\bar{A}(1-D) + \bar{B}(p/\sigma_0)^{\bar{N}} \right] \left[1 + \bar{C} \ln(\lambda/\dot{\varepsilon}_0) \right] \sigma_0, \quad (p/\sigma_0 > -\bar{T}), \quad (19)$$

where $3\lambda^2 = 2\hat{\mathbf{L}}^D : \hat{\mathbf{L}}^D$ for stresses exceeding the elastic limit, $\hat{\boldsymbol{\sigma}}$ is the deviatoric stress tensor. Material parameters from ref. [4] include \bar{A} , \bar{B} , \bar{C} , \bar{N} , $\dot{\varepsilon}_0$, and σ_0 , and \bar{T} is defined as $-\bar{p}/\sigma_0$, with \bar{p} the tensile pressure at failure. An isotropic inelastic response is assumed such that the inelastic spin may be neglected, meaning $\mathbf{L}^D = \mathbf{L}^{D,T}$. Note also that $\mathbf{L}^D \approx \dot{\mathbf{F}}^D \mathbf{F}^{D-1}$ when elastic shape changes are small. A 2D slice of the yield surface from (20) is shown in Fig. 2 for the particular case where $\Phi = \sigma_0$, where σ_1 and σ_2 are principle Cauchy stresses, and the third principle stress $\sigma_3 = 0$.

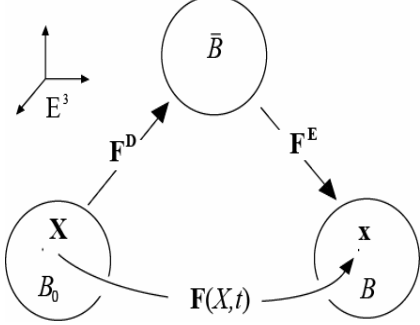


Fig. 1. Deformations and configurations.

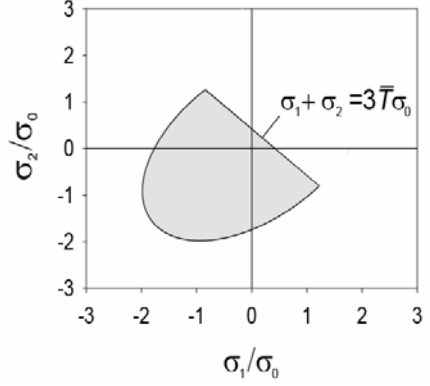


Fig. 2. HJC yield surface (2D).

The following kinetic equations dictate porosity and damage evolution:

$$\dot{\varphi} = \begin{cases} 0 & (p \leq p_c; p \geq p_L), \\ \hat{\alpha} \langle \dot{p} \rangle / \sigma_0 & (p_c < p < p_L), \end{cases} \quad \dot{D} = \hat{\kappa} \lambda \langle 1 - \pi_D(p/\sigma_0) \rangle + \bar{T}^{-1} \langle -\dot{p}/\sigma_0 \rangle, \quad (20)$$

where $\hat{\alpha}$, $\hat{\kappa}$, and π_D are positive constants, and the notation $2\langle x \rangle = x + |x|$. The pressure at which inelastic crushing commences is labeled p_c , and the locking pressure corresponding to p_L is denoted as p_L . Note that both $\dot{\varphi}$ and \dot{D} are always positive, i.e., irreversible.

The model is next demonstrated to be thermodynamically consistent. From (13)-(15),

$$-\rho \frac{\partial \psi}{\partial D} = J^{E-1} G \hat{\mathbf{E}}^E : \hat{\mathbf{E}}^E + J^{E-1} \frac{K_C^2 \omega_C}{2K_E}, \quad (21)$$

$$-\rho \frac{\partial \psi}{\partial \varphi} = J^{E-1} \left[\rho_0 \psi + K_E \vartheta_E^2 / 2\varphi_L - \left(K_1 / 2 + K_2 \vartheta_E / 3 + K_3 \vartheta_E^2 / 4 \right) \vartheta_E^2 / \varphi_L \right]. \quad (22)$$

Returning to (11), enforce the stronger requirements

$$\boldsymbol{\sigma} : \hat{\mathbf{L}}^D - \rho \frac{\partial \psi}{\partial D} \dot{D} + \left(\frac{p}{1+\varphi} - \rho \frac{\partial \psi}{\partial \varphi} \right) \dot{\varphi} \geq 0, \quad -\mathbf{q} \cdot \partial_x \theta \geq 0. \quad (23)$$

Then from (19) and (20),

$$\hat{\boldsymbol{\sigma}} : \hat{\mathbf{L}}^D = \lambda \hat{\boldsymbol{\sigma}} : \frac{\partial \Phi}{\partial \hat{\boldsymbol{\sigma}}} = \frac{\lambda}{2\bar{\sigma}} \hat{\boldsymbol{\sigma}} : \hat{\boldsymbol{\sigma}} \geq 0, \quad (24)$$

$$-J^E \rho \frac{\partial \psi}{\partial D} \dot{D} = \left[\frac{(\varphi_L - \varphi)}{2\varphi_L} K_E \vartheta_E^2 + G \hat{\mathbf{E}}^E : \hat{\mathbf{E}}^E + \frac{K_C^2 \omega_C}{2K_E} \right] \left[\hat{\kappa} \lambda \langle 1 - \pi_D(p/\sigma_0) \rangle + \bar{T}^{-1} \langle -\dot{p}/\sigma_0 \rangle \right] \geq 0, \quad (25)$$

meaning that the kinetic relations (19) and (20) are consistent with the laws of thermodynamics (23). Upon consideration of (22), the following constraint follows in terms of the pressure, since $\dot{\varphi} \geq 0$ from (20):

$$J^E \varphi_L p \geq (1 + \varphi_L) \left(K_1 / 2 + K_2 \vartheta_E / 3 + K_3 \vartheta_E^2 / 4 \right) \vartheta_E^2. \quad (26)$$

Material parameters are selected so (26) is satisfied over the model's range of applicability.

3. FRAGMENTATION

Two approaches for predicting fragment size and velocity statistics are derived in what follows. The first method, termed the 'energetic approach', relies on a local energy balance to determine the mean size and number of fragment(s) associated with each local volume element (e.g., a finite element, computational cell, or particle in a numerical context). The local velocity of that volume element is then assigned to all fragments. The second method, termed the 'statistical physics approach', is based upon maximization of a global statistical entropy function subject to constraints on conservation of mass, energy, and momentum. The premise of the latter method is that the most chaotic distribution consistent with the fundamental laws of mechanics and thermodynamics is deemed most favorable. Though not pursued here, the latter stochastic method could be used in conjunction with the energetic approach for describing subscale fragment distributions smaller than the grid size.

3.1 Energetic approach

Fragmentation of the local material element takes place over a time increment beginning when the damage reaches a threshold value, $D = D_T$. The energy released per unit volume over this time period due to internal micro-cracking is, from (15),

$$\rho e_D = \int_{D_T}^D \frac{K_C^2 \omega_C}{2K_E} dD = \frac{K_C^2 \omega_C}{2K_E} (D - D_T). \quad (27)$$

During the fragmentation event, the material retains all energy apart from e_D , which may be stored or dissipated as heat. Prior to fragmentation, energy released via Γ contributes to dissipation and temperature rise through (12); then, upon $D = D_T$, sufficient gaps between micro-cracks are assumed to have developed such that this energy is contributes to the relative kinetic energy of fragments. The energy transfer from the bulk constitutive model to fragment expansion then follows as

$$M \dot{e}_D = M \rho^{-1} \dot{\Gamma} \Big|_{D \geq D_T} = d \sum (u_l + u_s) / dt, \quad (28)$$

where M is the total mass of the volume element, and u_l and u_s denote absolute energy of the volume due to contributions from the relative linear and spin momentum per fragment. The progression of damage and fragmentation is illustrated in Fig. 3.

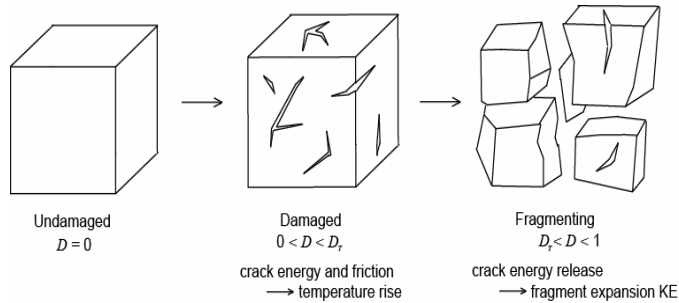


Fig. 3. Damage evolution and fragmentation processes.

For cube-shaped fragments with linear edge dimension b , energies in (28) can be estimated as

$$u_l = b^5 \rho \dot{\varepsilon}^2 / 16, \quad u_s = b^5 \rho \dot{\phi}^2 / 12, \quad (29)$$

where the scalar strain rate in the fragment is $\dot{\varepsilon} = \sqrt{\mathbf{D} : \mathbf{D}}$, with \mathbf{D} the symmetric part of \mathbf{L} , and $\dot{\phi}$ is the rate of rotation of the fragment about its moment of inertia. Derivation of the first of (29) follows that in [10]. Combining (28) and (29),

$$\left(\sum \rho b^3 \right) \dot{e}_D = \frac{d}{dt} \sum \left(b^5 \rho \dot{\varepsilon}^2 / 16 + b^5 \rho \dot{\phi}^2 / 12 \right). \quad (30)$$

Upon assuming equal and constant mass density among N fragments, replacing b with a median effective length $\bar{b}^3 = (\rho N)^{-1} M$, (30) is integrated to yield

$$\bar{b} = \sqrt{K_C^2 \omega_C (D - D_T) \left[K_E \rho \left(\dot{\varepsilon}^2 / 8 + \dot{\phi}^2 / 6 \right) \right]^{-1}}. \quad (31)$$

Equation (31) produces the mean fragment dimension \bar{b} . Mass conservation then provides the local number of fragments $N = M / (\rho \bar{b}^3)$.

3.2 Statistical physics approach

Here, the entire fragmenting body is considered at once, i.e., globally. The mass distribution is predicted via entropy maximization, subject to the constraints that the total mass and total number of fragments are known, following [11]. The constraints are written as

$$M = \rho \sum b^3 = \rho N \bar{b}^3, \quad (32)$$

where the mass density ρ is assumed the same among all fragments and the linear velocity does not affect the mass distribution. Quantities M and \bar{b} are determined from mass conservation and a global application of the preceding energetic analysis, respectively. The statistical entropy associated with the mass distribution is given by $S_M = k_B \ln P$, where k_B is Boltzmann's constant and P is the number of conceivable fragment arrangements. The value of S_M is maximized via maximization of the quantity [17]

$$\ln P = N \ln N - \sum_{i=0}^j n_i \ln n_i, \quad (33)$$

where n_i is the number of fragments of mass $m_i \leq m < m_i + \delta m_i$, with δm_i describing the range of masses admitted in each bin i , where j spans the total number of bins. Constraints (32) are rewritten as

$$N = \sum_{i=0}^j n_i, \quad M = \sum_{i=0}^j m_i. \quad (34)$$

Introducing Lagrange multipliers α and β , an equivalent function $f(n_i)$ is defined as

$$f = \ln P + \alpha \left(N - \sum n_i \right) + \beta \left(M - \sum m_i \right), \quad (35)$$

maximized by the solution of

$$\frac{\partial f}{\partial n_i} = -\left(1 + \ln n_i\right) - \alpha - \beta m_i = 0. \quad (36)$$

With the notation change $\alpha + 1 \rightarrow \alpha$, (36) yields

$$n_i = \exp(-\alpha - \beta m_i). \quad (37)$$

Rewriting (34) as integrals of continuous functions [11] gives

$$N = \int_0^\infty n dm = \int_0^\infty \exp(-\alpha - \beta m) dm = \exp(-\alpha)/\beta, \quad (38)$$

$$M = \int_0^\infty m n dm = \int_0^\infty m \exp(-\alpha - \beta m) dm = \exp(-\alpha)/\beta^2. \quad (39)$$

Finally, the mass probability distribution function (37) becomes

$$\hat{n}(m_i) = n_i = \left(N^2/M\right) \exp\left(-Nm_i/M\right). \quad (40)$$

The cumulative probability distribution of fragments larger than m is then

$$\hat{n}(m)/N = N_0 \exp(-N_0 m), \quad (41)$$

where $N_0 M = N$. Cumulative distribution (41) is shown in normalized form in Fig. 4(a).

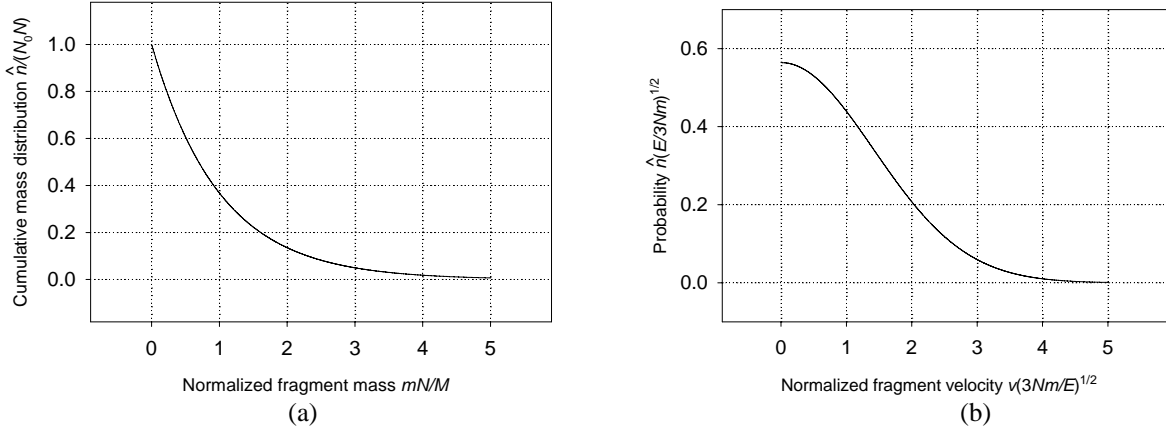


Fig. 4. Cumulative mass distribution (a) and velocity probability distribution (b), statistical physics model.

Analogously, the measure of statistical entropy of the fragment velocity distribution is $S_v = k_B \ln W$, attaining its greatest value upon maximization of

$$\ln W = N \ln N - \sum_{i=0}^j n_i \ln n_i, \quad (42)$$

where n_i is the number of fragments with kinetic energy $e_i \leq e < e_i + \delta e_i$, with δe_i describing the range of energies admitted in each bin i . Constraints on the fragment velocity distribution are

$$N = \sum_{i=0}^j n_i, \quad E = \sum_{i=0}^j e_i, \quad (43)$$

with E the total kinetic energy of the fragment cloud that will be determined later. Applying an analogous procedure as in (35)-(37), the velocity distribution takes the form

$$n_i = \exp(-\alpha - \beta e_i), \quad (44)$$

where Lagrange multipliers α and β are determined as follows. Let

$$\beta = 1/k_B T = 3N/2E, \quad (45)$$

where T is a thermodynamic temperature, via analogy with rigid molecules [17]. Assume that in ballistic scenarios the fragment velocity is coaxial with that of the center of mass of the fragment cloud, such that $2e_i = m_i v_i^2$. Then the velocity distribution may be expressed as

$$\hat{n}(v_i) = A \exp(-3Nm_i v_i^2 / 4E), \quad (46)$$

with $A = \exp(-\alpha)$ determined by normalization:

$$1 = \int_0^\infty \hat{n}(v) dv = A \int_0^\infty \exp(-3Nm v^2 / 4E) dv_i = A \sqrt{\pi E / 3mN}, \quad (47)$$

giving

$$\hat{n}(v) = \sqrt{3mN/\pi E} \exp(-3Nm v^2 / 4E). \quad (48)$$

The form (48) differs from that obtained by Grady & Winfree [12], who assumed fragments may scatter randomly in all directions, yielding 3D Maxwell-Boltzmann type velocity statistics. In the ballistic events simulated later, the flying debris tend to follow a path closer to one-dimensional than 3D or radial. Velocity probability distribution (48) is shown in normalized form in Fig. 4(b).

The joint probability distribution of mass and velocity is derived by combining (43) and (48):

$$\hat{p}(m, v) = \hat{n}(m) \hat{n}(v) = \sqrt{\frac{3mN^5}{\pi EM^2}} \exp\left[-m\left(\frac{N}{M} + \frac{3N}{4E}v^2\right)\right]. \quad (49)$$

Then,

$$\int_0^\infty \int_0^\infty \hat{p}(m, v) mv dm dv = \int_0^\infty m \hat{n}(m) \left(\int_0^\infty \hat{n}(v) v dv \right) dm = \sqrt{EM/3}. \quad (50)$$

Identifying (50) with the linear momentum of the fragment distribution, conservation of linear momentum dictates that the energy partitioned to the velocity distribution is

$$E = 3\rho \bar{b}^3 N \bar{v}^2. \quad (51)$$

Note that the expansion energy of (27) does not contribute to the velocity distribution because this energy is consumed by the strain and rotation rates of the fragments as indicated in (30).

4. CONCRETE: PARAMETERS AND IMPLEMENTATION

The preceding constitutive theory was applied to describe a concrete of unconfined compressive strength 48 MPa (7 ksi), as studied previously in [1, 4]. The fully crushed material is assumed to behave like the aggregate at high pressures, following Holmquist et al. [4]. Constants K_1 , K_2 , and K_3 , describing the volumetric elastic response of the fully crushed material, were determined by fitting the pressure-volume response of (17) to the

shock Hugoniot data for granite [18], assuming volumetric elastic deformation of the form $\mathbf{F}^E = (1 - \chi)\mathbf{1}$. Porosity evolution parameter $\hat{\alpha}$ was found via linear interpolation, i.e., $\hat{\alpha} = \varphi_L \sigma_0 / (p_L - p_C)$. Thermodynamic admissibility of porosity evolution, from (26), was verified numerically for all $\dot{\varphi} > 0$.

Fracture toughness K_C was obtained from ref. [19]. Following Sinha et al. [20], Hanchak et al. [1], and Holmquist et al. [4], failure occurs ($D = 1$) when the cumulative plastic strain $\lambda = 0.0033$ under null pressure conditions $p/\sigma_0 = 0$, giving $\hat{\kappa} = 300$. Similarly, following from data and analysis in the above references, prescribing $D = 1$ when $\lambda = 0.01$ under average pressure $p/\sigma_0 = 1/6$ yields $\pi_D = 4$.

Maximum crack density ω_C and threshold damage parameter D_T were chosen based on the assumption that the typical fragment size is on the order of the minimum dimension of the coarse aggregate of the concrete microstructure, here 9.5 mm. For cubic fragments, this implies an edge length \bar{b} of $9.5/\sqrt{3}$ mm. A typical strain rate observed over the duration of the fragmentation event was $\dot{\varepsilon} = 2(10)^4$ /s, based upon results of numerical analysis to be discussed later. With these values of \bar{b} and $\dot{\varepsilon}$, invoking (31) without spin, and assuming that fragmentation begins at the partially damaged state characterized by $D_T = 0.5$, gives the critical micro-crack density $\omega_C = 1.7(105)$ m⁻¹. Though the model functions adequately for the present investigation, more experiments and simulations are clearly needed to enable unique selection of parameters describing energetics of fracture and fragmentation over a range of loading rates, stress states, sample sizes, and concrete microstructures.

The deviatoric stress rate expression was derived by differentiating (16) and assuming small elastic stretch:

$$\dot{\boldsymbol{\sigma}} = 2G(1-D)\hat{\mathbf{D}}^E + \mathbf{W}^E\hat{\boldsymbol{\sigma}} - \hat{\boldsymbol{\sigma}}\mathbf{W}^E - \dot{D}\hat{\boldsymbol{\sigma}}/(1-D), \quad (52)$$

where $\hat{\mathbf{D}}^E$ is the symmetric and deviatoric part of \mathbf{L}^E and \mathbf{W}^E is the elastic spin (skew part \mathbf{L}^E). The small elastic strain assumption is thought to be justified for concrete deforming in shear or tension as yielding and failure of the material should occur prior to the attainment of large deviatoric stresses. At large pressures, the hydrostatic response is integrated in terms of the modified total volumetric strain $\bar{\mu}$, following the approach in [4]:

$$\bar{\mu} = (\mu - \varphi_L)/(1 + \varphi_L). \quad (53)$$

At pressures beneath the locking pressure, (17) is used, whereas a direct cubic fit to the Hugoniot data [18] is invoked at high pressures. Possible errors due to linearization of the elastic strain propagated from (52) are thus avoided in the hydrostatic response.

The energy balance (12) is exercised, along with thermodynamic expressions (22) and (25), to update the temperature and internal energy of the material. The elastic strain quantities of (5), and hence the elastic deformation gradient \mathbf{F}^E , are needed for this purpose. The latter is integrated numerically via [21]:

$$\mathbf{F}_{t+\Delta t}^E = \exp(\mathbf{L}^E \Delta t) \mathbf{F}_t^E, \quad (54)$$

where Δt is the time increment of integration.

The following methodology for addressing failure of the material is applied. When an integration point achieves a critical value of damage, $D = 1$, 'failure' occurs. Failed material supports no deviator stresses or tensile pressure. Finite elements are converted into particle

nodes when a scalar measure of strain, termed the 'erosion strain', is attained [7, 8]. In the calculations that follow, the erosion strain is chosen as 0.5, as recommended in [22].

Recall that two methods have been developed for predicting fragment mass and velocity distributions. For the approach of Section 3.1, a typical fragment dimension is computed for each converted particle using Eq. (31), where the strain rate $\dot{\varepsilon}$ during the fragmentation event is time-averaged only over integration cycles for which $D > D_r$. Each fragment is assigned the velocity of its parent particle. For the statistical physics-based approach of 3.2, the total mass and mass-weighted velocity of the particle cloud (see later Eq. (56)) are extracted from the simulation output. The total number of fragments follows from assumption of a nominal fragment dimension corresponding to the aggregate size as discussed above. Velocity and mass probability distributions are then calculated in a post-processing step.

5. BALLISTIC SIMULATION

The initial problem geometry is shown in Fig. 5, in which a tungsten sphere impacts a concrete plate at a normal striking velocity of 1120 m/s. Two meshes were considered, a coarse grid with 102144 composite tetrahedral elements [22] and a fine grid with 244512 elements. The analysis was conducted over 150 μs . Contact between projectile and target was assumed frictionless in the calculations. The alloy of the spherical projectile was modeled using the plasticity formulation of Johnson & Cook [5] with a Mie-Gruneisen equation-of-state for hydrostatics [22]. Failure of the tungsten material was suppressed.

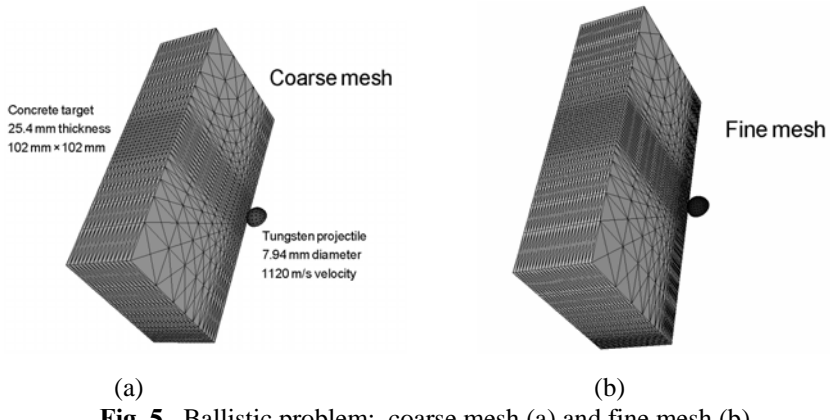


Fig. 5. Ballistic problem: coarse mesh (a) and fine mesh (b).

Results from the two simulations are compared quantitatively in Table 1. The hole diameter was estimated from the visible perforation. The crater diameter was estimated from the region surrounding the perforation where the material was fully damaged, i.e., where $D \approx 1$. Presumably such fully damaged material would simply fall off the target after the impact event due to gravimetric force, leaving behind a crater. The mass loss in the simulation was found from

$$M_L = \int \rho D dV , \quad (55)$$

where the domain of integration in (55) is the volume of target material. Eroded mass M reported in Table 1 was calculated as the summed mass of all particle nodes. The average velocity magnitude of the fragment cloud was computed by

$$\bar{v} = M^{-1} \sum_k m_k v_k , \quad (56)$$

with the velocity v_k of each particle k weighed by that particle's mass m_k .

Table 1. Numerical results.

	Model, coarse mesh	Model, fine mesh
Penetrator V_R [m/s]	814	825
Hole diameter [mm]	25	26
Crater diameter [mm]	52	50
Mass loss M_L [kg]	0.134	0.123
Eroded mass M [kg]	0.014	0.014
Avg. fragment speed \bar{v} [m/s]	133	116

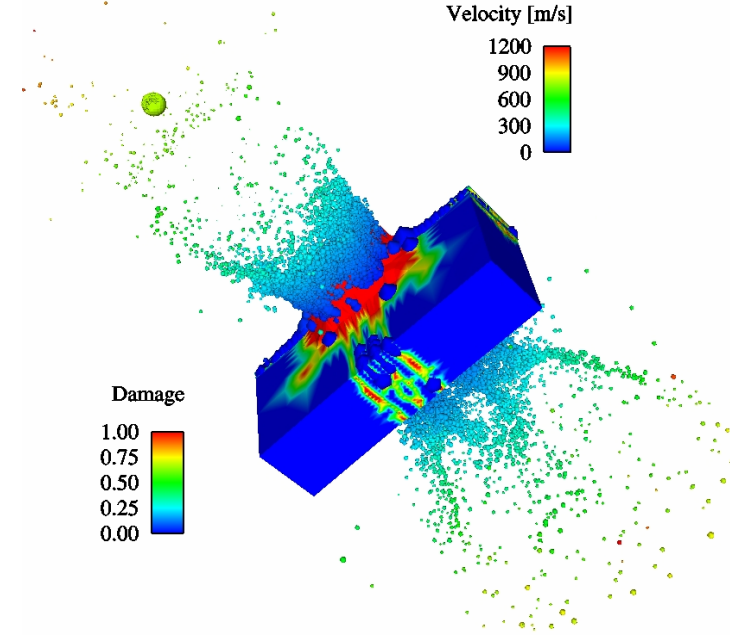


Fig. 6. Simulation at $150 \mu\text{s}$. Particles scaled by fragment diameter and colored by velocity magnitude. Target elements colored by damage D .

The coarse-meshed simulation, $150 \mu\text{s}$ after impact, is shown in Fig. 6. Corresponding results for the fine mesh were similar and are not shown. Concrete particles are scaled visually by the nominal fragment diameter \bar{b} , as computed from (32), assuming $\phi = 0$. Particles are colored by velocity magnitude. The projectile's exit velocity exceeds that of most of the particles. Larger fragments are slower-moving and remain close to the target, with smaller, faster-moving fragments in some cases outpacing the projectile. Contours of damage D are shown in the elements comprising target concrete material. The most damaged concrete logically surrounds the perforation, though the damage pattern is not purely axi-symmetric.

Mass probability distributions for the fragment cloud are shown in Fig. 7(a). The distributions were computed in two different ways: the energetic theory of 3.1 and the statistical physics-based theory of 3.2. For the former, the mass of fragments comprising a particle k was found from (31) as

$$m_k = \left[\frac{K_C^2 \omega_C (D - D_T)}{8 K_E \rho^{1/3} \dot{\varepsilon}^2} \right]_k^{3/2}. \quad (57)$$

Distributions were then constructed by grouping fragments into bins organized by mass:

$$\bar{p}(m_1 < m < m_2) = M^{-1} \sum_j m_j, \quad (58)$$

where j includes fragments with masses in the range $m_1 < m < m_2$. Probability distributions for the statistical theory were found from integrating Eq. (49) as follows:

$$\bar{p}(m_1 < m < m_2) = \frac{1}{M} \int_{m_1}^{m_2} \int_0^{\infty} m \hat{p}(m, v) dv dm = -\left(\frac{m}{M} + \frac{1}{N} \right) \exp\left(\frac{-N}{M} m \right) \Big|_{m_1}^{m_2}. \quad (59)$$

Minor differences in mass distributions among simulations with coarse and fine meshes are predicted by the energetic theory, a few percent at most for any bin. Since an identical value of eroded mass M was found in both simulations (Table 1), the statistical theory predictions were identical for coarse and fine grids.

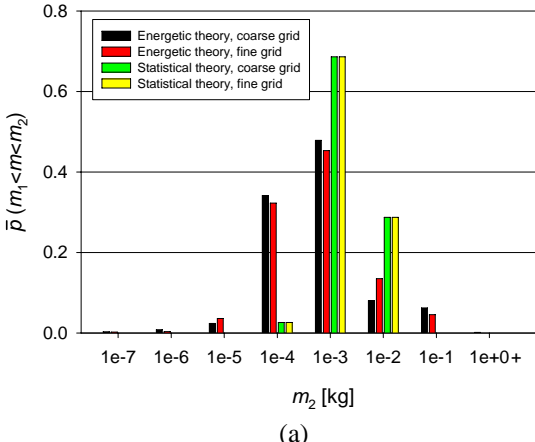
Velocity probability distributions are shown in Fig. 7(b). For the energetic theory, the magnitude of mass-weighted velocity probability for any particular bin was found from

$$\bar{p}(v_1 < v < v_2) = M^{-1} \sum_k m_k, \quad (60)$$

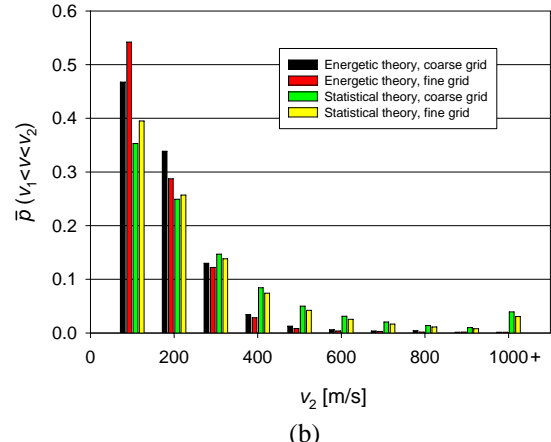
where k identifies a particle with velocity in the range $v_1 < v < v_2$, with mass m_k . For the statistical physics-based theory, the center of mass velocity \bar{v} of (56) and Table 1 was substituted into (51) to compute the global kinetic energy E . The probability was then estimated from (49) as

$$\bar{p}(v_1 < v < v_2) = N^{-1} \int_{v_1}^{v_2} \int_0^{\infty} \hat{p}(m, v) dm dv = \sqrt{3N/4E} \left(v / \sqrt{N/M + 3Nv^2/4E} \right) \Big|_{v_1}^{v_2}. \quad (61)$$

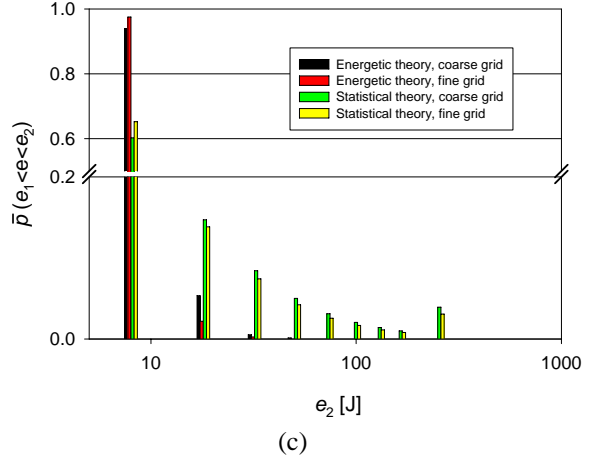
Figure 7(b) shows the predicted mass fraction of fragments within a particular velocity range. The bin of lowest velocities, with range $0 < v < 100$ m/s, was predicted, for both methods and both meshes, to contain the largest mass fraction of fragments.



(a)



(b)



(c)

Fig. 7. Predicted fragment mass (a), velocity (b), and kinetic energy (c) distributions at 150 μ s.

6. CONCLUSIONS

A constitutive framework has been formulated with the following features: finite deformation kinematics of elasticity, plasticity, and pore collapse; thermodynamic contributions from nonlinear elasticity, damage, and porosity; and kinetics consistent with both the energy balance and entropy inequality. Two thermodynamically motivated methods have been derived to compute fragment size and velocity distributions. The theory was implemented in a Lagrangian finite element setting with GPA, and was used to study the impact of a metal projectile upon a thin concrete barrier. Residual projectile velocities, hole and crater dimensions, and target mass loss were comparable between two simulations of different mesh density. Fragment debris characteristics appeared realistic, with the largest particles usually flying slowest. Fragment distributions were qualitatively similar among all model outputs, with the bin corresponding to the largest mass fraction of fragments having a particular mass, velocity, or kinetic energy range the same regardless of method or mesh size.

7. ACKNOWLEDGEMENT

This work was supported by the Weapons and Materials Research Directorate of the U.S. Army Research Laboratory.

REFERENCES

- [1] Hanchak, S.J., Forrestal, M.J., Young, E.R., and Ehrgott, J.Q., 1992. Perforation of concrete slabs with 48 MPa (7 ksi) and 140 MPa (20 ksi) unconfined compressive strengths. *Int. J. Impact Engng.* 12, 1-7.
- [2] Williams, E.M., Akers, S.A., and Reed, P.A., 2005. Laboratory characterization of fine aggregate cementitious material. *ERDC/GSL TR-05-16*, U.S. Army Corps of Engineers, Engineer Research and Development Center.
- [3] Momber, A.W., 2003. The efficiency of mechanical concrete comminution. *Eng. Fracture Mech.* 70, 81-91.
- [4] Holmquist, T.J., Johnson, G.R., and Cook, W.H., 1993. A computational constitutive model for concrete subjected to large strains, high strain rates, and high pressures. *Proc. 14th Int. Symp. Ballistics*, Quebec City, Canada, pp. 591-600.
- [5] Johnson, G.R. and Cook, W.H., 1983. A constitutive model and data for metals subjected to large strains, high strain rates, and high temperatures. *Proc. 7th Int. Symp. on Ballistics*, The Hague, Netherlands, pp. 541-547.
- [6] Johnson, G.R. and Cook, W.H., 1985. Fracture characteristics of three metals subjected to various strains, strain rates, temperatures, and pressures. *Engng. Fract. Mech.* 21, 31-48.
- [7] Johnson, G.R., Stryk, R.A., and Beissel, S.R., 1996. SPH for high velocity impact calculations. *Comp. Meth. Appl. Mech. Engng.* 139, 347-373.
- [8] Johnson, G.R., Holmquist, T.J., and Beissel, S.R., 2003. Response of aluminum nitride (including a phase change) to large strains, high strain rates, and high pressures. *J. Appl. Phys.* 94, 1639-1646.
- [9] Grady, D.E., 1982. Local inertial effects in dynamic fragmentation. *J. Appl. Phys.* 53, 322-325.
- [10] Johnson, G.R. and Cook, W.H., 1990. Recent EPIC code developments for high velocity impact: 3D element arrangements and 2D fragment distributions. *Int. J. Impact Engng.* 10, 281-294.
- [11] Grady, D.E. and Kipp, M.E., 1985. Geometric statistics and dynamic fragmentation. *J. Appl. Phys.* 58, 1210-1222.

- [12] Grady, D.E. and Winfree, N.A., 2001. Impact fragmentation of high-velocity compact projectiles on thin plates: a physical and statistical characterization of fragment debris. *Int. J. Impact Engng.* 26, 249-262.
- [13] Lee, E.H. and Liu, D.T., 1967. Elastic-plastic theory with application to plane-wave analysis. *J. Appl. Phys.* 38, 19-27.
- [14] Coleman, B.D. and Noll, W., 1963. The thermodynamics of elastic materials with heat conduction and viscosity. *Arch. Rat. Mech. Anal.* 13, 167-178.
- [15] Coleman, B.D. and Gurtin, M., 1967. Thermodynamics with internal state variables. *J. Chem. Phys.* 17, 597-613.
- [16] Grady, D.E., 1988. The spall strength of condensed matter. *J. Mech. Phys. Solids* 36, 353-384.
- [17] Lavenda, B.H., 1991. *Statistical Physics, A Probabilistic Approach*. Wiley, New York.
- [18] Marsh, S.P., 1980. *LASL Shock Hugoniot Data*. Univ. Calif. Press.
- [19] Lambert, D.E. and Ross, C.A., 2000. Strain rate effects on dynamic fracture and strength. *Int. J. Impact Engng.* 24, 985-998.
- [20] Sinha, B.P., Gerstle, K.H., and Tulin, L.G., 1964. Stress-strain relations for concrete under cyclic loading. *J. Amer. Concrete Inst.* 61, 195-210.
- [21] Clayton, J.D., 2005. Dynamic plasticity and fracture in high density polycrystals: constitutive modeling and numerical simulation. *J. Mech. Phys. Solids* 53, 261-301.
- [22] Johnson, G.R., Stryk, R.A., Holmquist, T.J., and Beissel, S.R., 1997. *Numerical algorithms in a Lagrangian hydrocode*. Alliant Techsystems, Inc., Hopkins, MN.

NO. OF
COPIES ORGANIZATION

1 DEFENSE TECHNICAL
(PDF INFORMATION CTR
ONLY) DTIC OCA
8725 JOHN J KINGMAN RD
STE 0944
FORT BELVOIR VA 22060-6218

1 US ARMY RSRCH DEV &
ENGRG CMD
SYSTEMS OF SYSTEMS
INTEGRATION
AMSRD SS T
6000 6TH ST STE 100
FORT BELVOIR VA 22060-5608

1 DIRECTOR
US ARMY RESEARCH LAB
IMNE ALC IMS
2800 POWDER MILL RD
ADELPHI MD 20783-1197

3 DIRECTOR
US ARMY RESEARCH LAB
AMSRD ARL CI OK TL
2800 POWDER MILL RD
ADELPHI MD 20783-1197

ABERDEEN PROVING GROUND

1 DIR USARL
AMSRD ARL CI OK TP (BLDG 4600)

NO. OF
COPIES ORGANIZATION

ABERDEEN PROVING GROUND

30 DIR USARL
AMSRD ARL CI
R NAMBURU
AMSRD ARL CI HC
P CHUNG
C CORNWELL
D GROVE
AMSRD ARL WM
T WRIGHT
J MCCUALEY
AMSRD ARL WM MD
B CHEESEMAN
G GAZONAS
AMSRD ARL WM TA
B LOVE
S SCHOENFELD
AMSRD ARL WM TC
R COATES
M FERMEN COKER
R PHILLABAUM
S SEGLETES
AMSRD ARL WM TD
J CLAYTON (5 CPS)
T BJERKE
T WEERASOORIYA
M GREENFIELD
H MEYER
D CASEM
M SCHEIDLER
M RAFTENBERG
D DANDEKAR
E RAPACKI
Y HUANG
S BILYK

INTENTIONALLY LEFT BLANK.